Title	Effect of different fuel NO models on the prediction of NO formation/reduction characteristics in a pulverized coal combustion field
Author(s)	Hashimoto, Nozomu; Watanabe, Hiroaki; Kurose, Ryoichi; Shirai, Hiromi
Citation	Energy, 118, 47-59 https://doi.org/10.1016/j.energy.2016.12.003
Issue Date	2017-01-01
Doc URL	http://hdl.handle.net/2115/72257
Rights	© 2017. This manuscript version is made available under the CC-BY-NC-ND 4.0 license http://creativecommons.org/licenses/by-nc-nd/4.0/
Rights(URL)	http://creativecommons.org/licenses/by-nc-nd/4.0/
Type	article (author version)
File Information	manuscript(HUSCAP).pdf

Effect of different fuel NO models on the prediction of NO formation/reduction characteristics in a pulverized coal combustion field

Nozomu HASHIMOTO[1,2*], Hiroaki WATANABE[1,3], Ryoichi KUROSE[4], Hiromi SHIRAI[1]

1. Energy Engineering Research Laboratory, Central Research Institute of Electric Power Industry (CRIEPI), 2-6-1 Nagasaka, Yokosuka, Kanagawa 240-0196 Japan
2. Division of Mechanical and Space Engineering, Hokkaido University, Kita 13, Nishi 8, Kita-ku, Sapporo, 060-8628 Japan
3. Department of Mechanical Engineering, Kyushu University, 744 Motooka, Nishi-ku, Fukuoka, 819-0395 Japan
4. Department of Mechanical Engineering and Science, Kyoto University, Yoshida-honmachi, Sakyo-ku, Kyoto 606-8501 Japan

* Correspondence: Nozomu HASHIMOTO

Laboratory of Space Utilization, Division of Mechanical and Space Engineering, Graduate School of Engineering, Hokkaido University, Kita 13, Nishi 8, Kita-ku, Sapporo, 060-8628 Japan

Phone: +81-11-706-6386

FAX: +81-11-706-6386

E-mail: nozomu.hashimoto@eng.hokudai.ac.jp

Abstract

To investigate the effects of fuel NO formation models on the prediction of NO concentrations in a coal combustion field, numerical simulations for a coal combustion field in a 760 kW test furnace were performed. Three models, those proposed by De Soete, Chen et al. and Mitchell et al. were employed to calculate fuel NO formation originating from volatile matter. The results show that the model proposed by Mitchell et al. reproduces the tendency of the experimental data better than the other two models. In addition, the difference between the NO conversion ratios of bituminous coal and sub-bituminous coal that contains a high level of moisture was examined in detail using simulation results from the model of Mitchell et al. It was found that the formation of a region with a low oxygen mole fraction immediately downstream of a region with a high NO production rate is essential to realize a low NO conversion ratio.

1. Introduction

Coal is an important energy resource from the viewpoint of energy security, because coal quarries and mines are prevalent in various regions all over the world and the number of coal deposits is greater than those of other fossil fuels. For electricity production, a large proportion of coal is consumed by coal-fired thermal power plants that employ the method of pulverized coal combustion. Therefore, emissions from pulverized-coal-fired thermal power plants represent a very important issue for the electric power industry. Although combustion technologies for reducing NOx emissions, such as staged combustion, have been utilized in pulverized-coal-fired plants [1], there is even greater potential for NOx emission reduction. NOx emissions from furnaces can be affected by fuel properties, boiler and burner design, and operating conditions. Recently, demand for utilizing low-grade coals or biomass fuels has increased due to factors such as the increased price of coal and global warming. Thus, the ability to predict changes in NOx emissions caused by utilizing these fuels in large scale boilers is required. Some experimental research has been conducted on the fundamental phenomena of NOx production during coal combustion [e.g., 2-4]. However, the prediction of NOx emissions in actual large-scale boilers requires an understanding of gas flow patterns, temperature, and gas-species concentrations. Numerical simulations of pulverized coal combustion fields are useful to archive such understanding [e.g., 5-28]. Recently, numerical simulations of actual large-scale boilers have been conducted by some researchers [e.g., 7-10]. Numerical simulations for predicting NOx formation characteristics in coal combustion fields have also been conducted [e.g., 11-28].

Since numerical simulation of pulverized coal combustion fields is difficult due to the complexity of coal combustion phenomena, relatively simple models are generally employed. Particularly when simulating a combustion field in a large scale boiler, simplified models are mostly employed due to computational limitations even though there exist many precise models using large computational resources. Therefore, in common with other models, simplified NOx formation models are commonly used to predict NOx concentrations in large-scale boilers by numerical simulation of coal combustion fields. To simulate NOx concentrations in coal combustion fields, the calculation of various NOx formation mechanisms, i.e., the Zeldovich, prompt, and fuel NOx mechanisms, is required. Among these, fuel NOx mechanisms are the most important in coal combustion fields because large portions of the NOx emitted from furnace exits originate from fuel NOx mechanisms [29]. The fuel NOx mechanisms are divided into those for which NOx originates from volatile matter and those for which it originates from char particles. For numerical simulations of coal combustion fields in large-scale boilers, the simple NOx

1

29　formation model proposed by De Soete [30] is commonly employed for NOx originates from volatile matter [e.g.,

30　21-28]. However, there are other simple NOx formation models, for instance, Chen et al. [31] made corrections of

31　the reaction parameters of De Soete's model based on the experimental data and recommended the use of proposed

32　parameters instead of the original parameters. Mitchell et al. [32] proposed a simple NOx formation model that

33　employed ammonia as an intermediate spices. Use of the models proposed by Chen et al. and Mitchell et al. for

34　numerical simulation of coal combustion fields is expected to improve the accuracy of NOx emission prediction.

35　However, investigations of the differences in NOx formation characteristics between simulations employing these

36　fuel NOx formation models have not yet been reported.

37　　In this study, numerical simulations for the coal combustion field in a 760 kW test furnace were performed using

38　three models for the formation of fuel NOx originating from volatile matter, i.e., the models proposed by De Soete

39　[30], Chen et al. [31] and Mitchell et al. [32]. The NOx formation characteristics of each of these three simulations

40　were compared in detail. In addition, differences in the NO emission characteristics between the combustion fields

41　of bituminous coal and sub-bituminous coal that contains a high level of moisture are discussed.

42

43　**2. Numerical simulation**

44　**2.1. NOx formation model**

45　　In this study, only the production of NO was taken into account because the NOx emitted from an atmospheric

46　pulverized coal combustion field consists mostly of NO, with much lower concentrations of NO_2 and N_2O. In this

47　study, the NO formation models were employed in a "post-processing" fashion, in which a converged combustion

48　flow field solution is obtained before performing the NO prediction. To predict the NO concentration in a coal

49　combustion field, the consideration of four main NO formation mechanisms, i.e., the extended Zeldovich NO

50　mechanism, the prompt NO mechanism, the fuel NO mechanism originating from volatile matter, and the fuel NO

51　mechanism originating from char particles, is required. In this study, three NO formation models were employed and

52　the NO formation characteristics predicted by the three models were compared. Table 1 shows a summary of the

53　three models. For the fuel NO formation mechanism originating from volatile matter, the models proposed by De

54　Soete [30] (Model 1), Chen et al. [31] (Model 2) and Mitchell et al. [32] (Model 3), were employed. For the other

55　NO formation mechanisms, i.e., the Zeldovich NO mechanism, the prompt NO mechanism, and the fuel NO

56　formation mechanism originating from char particles, the same equations were used for all three models. The N

2

57 partition ratio between volatile-N and char-N was determined by the modified-TDP model [43] based on the

58 devolatilization database made by the FLASHCHAIN model [52, 53]. The same value of the N partition ratio

59 derived from the modified TDP model was used for all fuel NO formation models listed in Table 1. Detailed

60 explanations of each NO mechanism are described in the following sections.

61
62 **2.1.1. Extended Zeldovich NO model**

63 To calculate NO production by using the extended Zeldovich NO mechanism, the following formulae are

64 employed:

65

66
$$N_2 + O \underset{K_{-1}}{\overset{K_1}{\rightleftharpoons}} NO + N,$$
(2.1)

67
$$N + O_2 \underset{K_{-2}}{\overset{K_2}{\rightleftharpoons}} NO + O,$$
(2.2)

68
$$N + OH \underset{K_{-3}}{\overset{K_3}{\rightleftharpoons}} NO + H,$$
(2.3)

69

70 where K_i denotes various reaction rate parameters. By employing the quasi-steady-state approximation for the N

71 radical, the NO production rate can be expressed by

72

$$
\frac{d[NO]}{dt} = \frac{\rho_g^2}{1 + \left(K_{-1}\dfrac{Y_{NO}}{M_{NO}}\right) \bigg/ \left(K_2\dfrac{Y_{O_2}}{M_{O_2}} + K_3\dfrac{Y_{OH}}{M_{OH}}\right)}
$$

73
$$
\times \left[2K_1\frac{Y_O}{M_O}\frac{Y_{N_2}}{M_{N_2}} - \frac{2K_{-1}\dfrac{Y_{NO}}{M_{NO}}}{K_2\dfrac{Y_{O_2}}{M_{O_2}} + K_3\dfrac{Y_{OH}}{M_{OH}}}\left(K_{-2}\frac{Y_O}{M_O}\frac{Y_{NO}}{M_{NO}} + K_3\frac{Y_H}{M_H}\frac{Y_{NO}}{M_{NO}}\right) \right],
$$
(2.4)

74

75 where Y_i and M_i denote the mass fraction and molecular weight of species i, respectively. In this study, the following

76 reaction rate parameters, proposed by Baulch et al. [33], are employed for K_i in the above formula:

77

78
$$K_1 = 1.8 \times 10^{11} \exp\left(\frac{-38370}{T_g}\right),$$
(2.5)

79 $$K_{-1} = 3.8 \times 10^{10} \exp\left(\frac{-425}{T_g}\right),$$ (2.6)

80 $$K_2 = 1.8 \times 10^7 \exp\left(\frac{-4680}{T_g}\right),$$ (2.7)

81 $$K_{-2} = 3.8 \times 10^6 \exp\left(\frac{-20820}{T_g}\right),$$ (2.8)

82 $$K_3 = 7.1 \times 10^{10} \exp\left(\frac{-450}{T_g}\right),$$ (2.9)

83 $$K_{-3} = 1.7 \times 10^{11} \exp\left(\frac{-24560}{T_g}\right),.$$ (2.10)

84

85 In this study, the effects of OH and H radicals in Eq. (2.4) were ignored. The following equation, proposed by

86 Westenberg [34], was employed to calculate the mass fraction of the O radical in Eq. (2.4):

87

88 $$Y_O = \frac{M_O}{\rho_g}\left(\rho_g \frac{Y_{O_2}}{M_{O_2}}\right)^{0.5} \frac{3.97 \times 10^5}{T_g^{0.5}} \exp\left(-\frac{31090}{T_g}\right).$$ (2.11)

89

90 **2.1.2. Prompt NO model**

91 To calculate NO production by the prompt NO mechanism, the following formula, proposed by De Soete [30],

92 was employed:

93

94 $$\frac{d[NO]}{dt} = 1.2 \times 10^7 X_{O_2}^b X_{N_2} X_{fuel} \exp\left(\frac{-2.512 \times 10^5}{RT_g}\right)\frac{P_g}{RT_g},$$ (2.12)

95

96 where X_i denotes the mole fraction of species i and b is expressed by the following formulae:

97

98 $$b = 1.0, \left(X_{O_2} < 4.1 \times 10^{-3}\right),$$ (2.13)

99 $$b = -3.95 - 0.9 \ln X_{O_2}, \left(4.1 \times 10^{-3} \leq X_{O_2} < 1.11 \times 10^{-2}\right),$$ (2.14)

100 $$b = -0.35 - 0.1 \ln X_{O_2}, \left(1.11 \times 10^{-2} \leq X_{O_2} < 3.0 \times 10^{-2}\right),$$ (2.15)

101 $$b = 0, \left(3.0 \times 10^{-2} \leq X_{O_2}\right).$$ (2.16)

2.1.3. Models for NO originating from volatile matter

NO production originating from volatile matter is considered to be very important in pulverized coal combustion fields. For NO production originating from volatile matter, the model proposed by De Soete [30] is commonly employed in numerical simulations of coal combustion fields [21-28]. However, in the detailed chemical reaction simulation conducted by Pederson et al. [35], is was found that the overall reaction rate in the model proposed by De Soete tends to underestimate NO concentration in a low oxygen concentration environment. Therefore, in this study, three models for fuel NO production originating from volatile matter, i.e., the models proposed by De Soete [30] (Model 1), Chen et al. [31] (Model 2) and Mitchell et al. [32] (Model 3), were employed. The differences between the NO formation characteristics of these models were compared in detail.

2.1.3.1 De Soete's model (Model 1)

Figure 1 (a) shows a schematic of the model proposed by De Soete [30]. In this model, HCN evolved from coal particles as volatile matter is consumed by two competing reactions: one producing NO by reaction with O_2 and the other producing N_2 by reaction with NO. The reaction rates can be expressed by the following equations:

$$\frac{d[HCN]}{dt} = -1.0 \times 10^{10} X_{HCN} X_{O_2}^{b} \exp\left(\frac{-2.805 \times 10^{5}}{RT_g}\right) \frac{P_g}{RT_g}, \quad (2.17)$$

$$\frac{d[HCN]}{dt} = -3.0 \times 10^{12} X_{HCN} X_{NO} \exp\left(\frac{-2.512 \times 10^{5}}{RT_g}\right) \frac{P_g}{RT_g}, \quad (2.18)$$

where b can be calculated by using Eqs. (2.13) – (2.16).

2.1.3.2 Chen et al.'s model (Model 2)

Chen et al. conducted chemical reaction simulations with elementary kinetics and compared simulation results with experimental data [31]. They found that employing the following equations, instead of the original equations from De Soete, provided a better prediction:

$$\frac{d[HCN]}{dt} = -1.5 \times 10^{10} X_{HCN} X_{O_2}^{b} \exp\left(\frac{-2.646 \times 10^{5}}{RT_g}\right) \frac{P_g}{RT_g}, \quad (2.19)$$

129
$$\frac{d[HCN]}{dt} = -1.1 \times 10^{12} \, X_{HCN} X_{NO} \exp\left(\frac{-2.454 \times 10^5}{RT_g}\right) \frac{P_g}{RT_g} . \qquad (2.20)$$

130

131 **2.1.3.3 Mitchell et al.'s model (Model 3)**

132   Figure 1 (b) shows a schematic of the model proposed by Mitchell et al. [32]. In this model, HCN is converted to

133 NH_3, followed by the reactions of NH_3 to NO and N_2. The reaction rates are expressed by the following equations:

134

135
$$\frac{d[HCN]}{dt} = -1.94 \times 10^{15} \, X_{HCN} X_{O_2} \exp\left(\frac{-3.282 \times 10^5}{RT_g}\right) \frac{P_g}{RT_g} , \qquad (2.21)$$

136
$$\frac{d[NH_3]}{dt} = \frac{-3.48 \times 10^{20} \, X_{NH_3} X_{O_2} \exp\left(-4.186 \times 10^5 / RT_g\right)}{1 + 6.90 \times 10^{-6} \, X_{O_2} \exp\left(1.758 \times 10^5 / RT_g\right)} \frac{P_g}{RT_g} , \qquad (2.22)$$

137
$$\frac{d[NH_3]}{dt} = -6.22 \times 10^{14} \, X_{NH_3} X_{NO} \exp\left(\frac{-2.302 \times 10^5}{RT_g}\right) \frac{P_g}{RT_g} , \qquad (2.23)$$

138
$$\frac{d[HCN]}{dt} = 1.00 \times 10^4 \, X_{NO} X_{CmHb} \frac{P_g}{RT_g} , \qquad (2.24)$$

139

140 where X_{CmHb} in Eq. (2.24) is the mole fraction of gaseous hydrocarbons, which is represented by CH_3 [36]. In this

141 study, the concentration of gaseous hydrocarbons could not be calculated in detail because the volatile matter was

142 treated as a mixture of postulated substances; therefore, its detailed reaction chemistry of the volatile matter could

143 not be effectively quantified. However, it was considered that the concentration of gaseous hydrocarbons is

144 correlated with that of volatile matter. Therefore, the concentration of hydrocarbons was assumed to be proportional

145 to that of volatile matter according to the following formula:

146

147
$$X_{CmHb} = C_1 X_{VM} , \qquad (2.25)$$

148

149 where X_{VM} is the mole fraction of volatile matter, and C_1 is a constant. The value of C_1 was set to 1×10^{-2} in this study.

150 The effect of the value of C_1 on NO formation is discussed in the section 3.1.

151

152 **2.1.4. Model for NO production originating from char particles**

153   To calculate NO production originating from char particles, the following formula, proposed by Lockwood et al.

154   [37], was employed:

155

156    $$S_{NO,Ch} = -\frac{dC}{dt} m_{N,Ch} F_c \eta_{N,Char} ,$$ (2.26)

157

158   where $\eta_{N,Char}$ is the conversion factor of the nitrogen in the char to NO; it was set to 0.2 in this study.

159

160   **2.1.5. Model for NO reduction by char particles**

161   The NO-char reaction has been investigated by various researchers [38-41] and is believed to have a large effect on

162   NO reduction in a pulverized coal combustion environment. The rate of NO reduction by char can be calculated by

163   the following equation:

164

165    $$\frac{d[NO]}{dt} = -A_{re} X_{NO} \exp\left(-\frac{E_{re}}{RT_p}\right) S_p \frac{P_g}{RT_g} ,$$ (2.27)

166

167   where E_{re} was set to 1.33×10^6 J/mol (after Aarna et al. [38], who obtained this value by averaging the data from

168   various studies). S_p is the external surface area of char particles per unit volume (m^2/m^3). The pre exponential factor,

169   A_{re}, is was to 2.0×10^4 m/s in this study.

170

171   **2.2. Comparison of NO production/reduction rates between the three volatile fuel NO models**

172   Before conducting the numerical simulation, the NO production/reduction rates of the three volatile fuel NO

173   models as functions of the O_2 mole fraction, the NO mole fraction, and the gas temperature were examined, as

174   shown in Fig. 2. The basic conditions for the calculations were: HCN concentration, 3000 ppm; volatile matter

175   concentration (VM), 10%; NO concentration, 100 ppm; and gas temperature, 1800 K. As can be understood from

176   Eqs. (2.17) – (2.24) and Fig. 1, the volatile fuel NO mechanisms have both production and reduction rates. The NH_3

177   concentration is required to calculate the NO production and reduction rates in Model 3 (Mitchell et al.), whereas it

178   is not required for Models 1 and 2. However, the NH_3 consumption rates for production and reduction (Eqs. (2.22)

179   and (2.23)) are much higher than the consumption rate of HCN (Eq. (2.21)). Consequently, the concentration of NH_3

180   is much lower than that of HCN [35]. Considering this fact, the steady-state approximation [42] for NH_3 was

7

181   adopted in this calculation, i.e., it was assumed that the overall NO production and reduction rates were controlled

182   by the HCN consumption rate (Eq. (2.21)). This steady-state approximation was only adapted to the calculation for

183   Fig. 2, and was not adapted to the numerical simulation for the coal combustion field in the 760 kW test furnace.

184   The ratio of the NO production rate to the NO reduction rate was calculated by using Eqs. (2.22) and (2.23) with

185   same value of NH_3 concentration. In Fig. 2, the solid and dotted lines indicate the production and reduction rates,

186   respectively, for Model 1 (blue), Model 2 (green), and Model 3 (red). If the solid line is higher than the dotted line,

187   the net NO production rate is positive. Conversely, if the dotted line is higher than the solid line, the net NO

188   production rate is negative. In Figs. 2 (a) and 2 (b), the NO production/reduction rates as a function of the O_2 mole

189   fraction at different gas temperatures are compared. The net NO production rate increases with increasing O_2 mole

190   fraction and switches from negative to positive at a certain O_2 mole fraction (intersection point of the solid and

191   dotted lines) for all three models. Throughout the range of O_2 mole fractions in Figs. 2 (a) and 2 (b), the order of the

192   net NO production rate is Model 1 < Model 2 < Model 3. However, there is no significant difference between the

193   models in terms of the overall trend. In Figs. 2 (c) and 2 (d), the NO production/reduction rates as a function of the

194   NO mole fraction at different O_2 concentrations are compared. For all three models, the NO reduction rate increases

195   with increasing NO mole fraction. As can be understood from Eqs. (2.17) and (2.19), the NO production rate for

196   Models 1 and 2 are unchanged with NO mole fraction, whereas the NO production rate decreases with increasing

197   NO mole fraction. However, there is no significant difference between the models in terms of the overall trend.

198   Throughout the range of NO mole fractions in Figs. 2 (c) and 2 (d), the order of the net NO production rate is Model

199   1 < Model 2 < Model 3. Figures 2 (e) and 2 (f) show the NO production/reduction rates as functions of gas

200   temperature at different O_2 concentrations. There is a significant difference between Model 3 and Models 1 and 2 in

201   terms of the overall trend. There is no significant difference between the shapes of the curves of NO production and

202   reduction rates for Models 1 and 2. Consequently, the NO production and reduction curves do not intersect for

203   Models 1 and 2 in Fig. 2 (f), i.e., the net NO production rates for Models 1 and 2 are negative throughout the gas

204   temperature range in Fig 2 (f). On the other hand, the shapes of the curves of NO production and reduction rates for

205   Model 3 are totally different. Consequently, there is an obvious intersection point between the NO production and

206   reduction rate curves for Model 3 in Fig. 2 (f), i.e., the net NO production rate switches from negative to positive at

207   around 1350 K with the increase in gas temperature. This large difference between the models in terms of the overall

208   trend with gas temperature change causes the significant difference in NO concentration distribution in the furnace,

209 as discussed later. The order of the net NO production rate at low gas temperature is Model 3 < Model 1 < Model 2,

210 whereas that at high gas temperature it is Model 1 < Model 2 < Model 3.

211

212 **2.3. Numerical methods**

213 Other than the NO formation model, the models used in this study for numerical simulation of the pulverized coal

214 combustion field were the same as those of Hashimoto et al. [43]. The models for the main phenomena are

215 summarized in Table 2.

216 The gas-phase time-averaged continuity equation and conservation equations of momentum, turbulent kinetic

217 energy, dissipation, enthalpy and species are

218

219 $$\frac{\partial}{\partial x_i}\left(\rho_g u_i\right) = S_c \,,$$ (2.28)

220 $$\frac{\partial}{\partial x_i}\left(\rho_g u_i \phi\right) = \frac{\partial}{\partial x_i}\left(\Gamma_\phi \frac{\partial \phi}{\partial x_i}\right) + S_\phi + S_{p\phi} \,,$$ (2.29)

221

222 where S_c denotes the mass source term from the representative particles to the gas phase. ϕ denotes the generalized

223 variables expressing the fluid velocity components u_i, the turbulent kinetic energy k, the rate of eddy dissipation ε,

224 the fluid enthalpy h and the mass fraction of chemical species Y_i. Γ_ϕ denotes the turbulent exchange coefficient, and

225 S_f and $S_{p\phi}$ represent the gas-phase source terms that exist in addition to the convection and diffusion terms and the

226 particle-phase source terms, respectively. The continuity and momentum equations were solved using the

227 pressure-implicit with splitting of operators (PISO) algorithm [50].

228 The mass of the representative coal particles m_p was calculated using the following equation by considering the

229 evaporation of moisture, the evolution of volatile matter by devolatilization and the evolution of carbon monoxide

230 by the char combustion from the particles:

231

232 $$\frac{dm_p}{dt} = \frac{dm_{moist}}{dt} + \frac{dm_{vola}}{dt} + \frac{dm_{char}}{dt}$$ (2.30)

233

234 where, m_{moist}, m_{vola} and m_{char} are the mass of moisture, volatile matter and fixed carbon in the particle, respectively.

235 The decrease rates of m_{moist}, m_{vola} and m_{char} were calculated by the modified TDP model [43] and the char

236 combustion model proposed by Field et al. [47] with the char combustion zone transition proposed by Essenhigh et

237 al. [47], as listed in Table 2.

238 The equation of motion for the representative coal particles is given by

239

240 $$m_p \frac{du_{pi}}{dt} = \frac{1}{2} C_d \rho_p A_p \mid u_{fi} - u_{pj} \mid (u_{fi} - u_{pi}), \qquad (2.31)$$

241 $$C_d = 24(1 + 0.15 \text{Re}_p^{0.687}) / \text{Re}_p , \qquad (2.32)$$

242 $$\text{Re}_p = D_p \mid u_{fi} - u_{pi} \mid / \nu . \qquad (2.33)$$

243

244 The particle temperature T_p was calculated using the following equation by considering the heat transfer due to

245 convection, radiation, heat loss due to the evaporation of moisture and the devolatilization reaction in the coal

246 particle, and heat gain due to char combustion:

247

248 $$m_p c_{p,p} \frac{dT_p}{dt} = -A_s h(T_p - T_g) + A_s \varepsilon_p \sigma (\Theta_R^{\ 4} - T_p^{\ 4}) + \Delta h_{lat} \frac{dm_{p,w}}{dt} + \Delta h_{dev} \frac{dm_{p,v}}{dt} + \dot{q}_{char} , \quad (2.34)$$

249 $$h = k_g Z (2 + 0.6 \text{Re}_p^{1/2} \text{Pr}^{1/3}) / (e^Z - 1) D_p , \qquad (2.35)$$

250 $$Z = -c_{p,g} (dm_p / dt) / \pi D_p k_g (2 + 0.6 \text{Re}_p^{1/2} \text{Pr}^{1/3}), \qquad (2.36)$$

251 $$\Theta_R = (I / 4\sigma)^{1/4} . \qquad (2.37)$$

252

253 The absorptivities of the coal particles and wall were assumed to be 0.85 and 0.4, respectively. Also, the absorption

254 coefficient of the gas was set at 0.075. The interaction of the conserved properties between the gas phase and the

255 coal particles was calculated by the particle-source-in cell (PSI-Cell) technique [51].

256 In this study, the modified tabulated-devolatilization-process (TDP) model [43] was employed for devolatilization

257 of the coal particle. The FLASHCHAIN model [52, 53] was used to produce the devolatilization database for the

258 TDP model.

259 Gaseous combustion between the volatile matter and air was calculated using a combined model of the kinetics and

260 eddy dissipation models [46]. The chemical mechanism consists of the following global reactions:

261

262 $\quad$ $VM + \alpha O_2 \rightarrow \beta CO + \gamma H_2 O$, $\qquad\qquad\qquad\qquad\qquad$ (2.38)

263 $\quad$ $CO + O_2 \rightarrow CO_2$. $\qquad\qquad\qquad\qquad\qquad\qquad\qquad$ (2.39)

264

265 $\quad$ In this study, the parameters proposed by Westbrook et al. [54] for C_7H_8 oxidation were employed for the rate

266 parameters regarding the kinetics in Eq. (2.38). The parameters proposed by Hautman et al. [55] for CO oxidation

267 were employed for the rate parameters regarding the kinetics in Eq. (2.39).

268

269 **2.4. Computational domain and conditions**

270 $\quad$ The test furnace studied here is located at the Energy Engineering Research Laboratory of CRIEPI, in which an

271 advanced low-NOx burner (CI-α burner [3]) with a coal combustion capacity of about 100 kg/h is installed. The

272 furnace is a water-cooled furnace made of steel with refractory materials placed on the inside wall. The diameter and

273 length of the furnace are 0.85 m and 8 m, respectively. The configuration of the computational domain is shown in

274 Fig. 3. The domain was designed to match the actual configuration accurately. The computational domain was half

275 of the furnace, and a periodic condition was applied in the azimuthal direction. Combustion air was injected into the

276 furnace through the burner and staged combustion air ports located 3.0 m from the burner outlet. The air passing

277 through the burner was divided into primary, secondary, and tertiary air. The primary air, which carries pulverized

278 coal, had straight motion. The secondary and tertiary air had strong swirling motions. The swirl vane angles for the

279 secondary and tertiary air were set to 81 deg. and 63 deg., respectively, which are the optimum values for

280 bituminous coal (these values are zero when the swirl force is zero).

281 $\quad$ The operating conditions of the furnace in the simulation were set to correspond with those in our experiment [56].

282 The thermal input of the coal combustion test furnace was 760 kW (the feed rate for bituminous coal was

283 approximately 100 kg/h). The excess air ratio was 1.24, and the O_2 mole fraction at the furnace outlet was 4.0%. The

284 staged combustion air ratio was set to 30%. The mass ratio of the pulverized coal (dry base) to the primary air was

285 1:2.2, and the mass ratio of secondary air to tertiary air was 1:6. The temperature of the primary air was set to 353 K,

286 and that of the secondary and tertiary air was 598 K. Regarding the boundary condition on the wall, the temperature

287 outside the furnace was assumed to be 308 K and thermal resistance was set to 0.04 (m^2 s K)/J.

288 $\quad$ The properties of the coals are listed in Table 3. The size distributions of coal particles used in the experiment [56]

289　　are shown in the Fig. 4. It was assumed that the pulverized coal consisted of particles with initial diameters of 5, 20,

290　　40, 60, 80, and 100 μm. The mass fractions of the coal particles were set to correspond with the actual particle size

291　　distribution in the experiment.

292　　　Four cases with different sub-bituminous coal mixing ratios were performed in this study, as listed in Table 4.

293　　Numerical simulations with sub-bituminous coal mixing ratios of 0%, 25%, 75% and 100% were conducted. The

294　　total thermal input was set at 760 kW for all cases, as described above. For each case, the calculations listed in Table

295　　1 were conducted for the three models. Therefore, a total of 12 calculations were conducted.

296

297　　**3. Results and discussion**

298　　**3.1. Effect of fuel NO model**

299　　　Figure 5 shows the simulation results of the gas velocity vectors, gas temperatures and O_2 mole fractions for

300　　Cases 1 and 4. For the gas velocity vectors, the colors in (a-1) and (a-2) indicate axial velocity. Also shown are the

301　　distributions of the gas temperature measured by the thermocouple and O_2 mole fraction measured during the

302　　experiments by a gas analyzer with a suction probe [56]. The radiative heat loss from the thermocouple was not

303　　corrected because of the difficulty of estimating the furnace wall temperature. The tendency of the simulation results

304　　is consistent with that of the experimental results. For instance, due to the large flame lift-off, the temperatures near

305　　the burner exit for both the simulation and experimental results in Case 4 (Fig. 5 (b-2) and (c-2)) are markedly lower

306　　than that in Case 1 (Fig. 5 (b-1) and (c-1)). Similarly, the oxygen mole fractions near the burner exit for both the

307　　simulation and experimental results in Case 4 (Fig. 5 (d-2) and (e-2)) are high, whereas that in Case 1 (Fig. 5 (d-1)

308　　and (e-1)) is low. These marked differences between the gas temperatures and oxygen mole fractions in Cases 1 and

309　　4 are due to the large flame lift-off for Case 4, as discussed in detail in Ref. [43]. It should be noted that because of

310　　the large flame lift-off for Case 4, there is a large difference between the gas velocity vector fields in Cases 1 and 4.

311　　　Figure 6 shows the effect of C_l in Eq. (2.25) for Model 3 on NO mole fraction at the furnace exit. The NO mole

312　　fraction at the furnace exit decreases with increasing C_l. Even though the absolute predicted values of the NO mole

313　　fraction with $C_l = 1$ for Case 1 and 2 agree well with the measured data, the simulation with $C_l = 1$ could not

314　　reproduce the increase in NO mole fraction with increasing Wara coal mixing ratio. The simulation with $C_l = 1 \times 10^{-4}$

315　　overestimates NO mole fraction too much. Therefore, $C_l = 1 \times 10^{-2}$ was used in Model 3 in all of the following

316　　discussion.

317   Figure 7 shows the NO mole fraction at the furnace exit as a function of Wara coal mixing ratio. In addition to the

318   simulation results from the three different volatile fuel NO models, the measurement results of the experiment [56]

319   are also shown. The NO mole fraction at the furnace exit of the experiment gradually increases with an increase in

320   the Wara coal mixing ratio. The NO mole fractions for Models 2 and 3 increase with increasing Wara coal mixing

321   ratio, whereas that for Model 1 decreases as this ratio increases. If only Fig. 7 is considered, it may appear that

322   Model 2 yields better results than the other models do. However, this appearance may change if the distribution of

323   the NO mole fraction in the furnace is also considered, as discussed below.

324   Figure 8 shows the distribution of the NO mole fraction on the central axis of the furnace. Model 3 yields the best

325   NO mole fraction of the models. Although overestimations of the NO mole fraction at $Z = 0.1$ m by Model 3 are

326   observed for (a) Case 1 (100% Newlands) and (b) Case 2 (75% Newlands + 25% Wara), the overall discrepancy for

327   Model 3 is smaller than that of the other models. Models 1 and 2 underestimate the NO mole fraction at the burner

328   zone (from $Z = 0$ m to 3 m).

329   Figures 9 show the two dimensional distributions of the NO mole fraction for Cases 1 and 4. From the figure, it is

330   evident that Model 3 yields a better NO mole fraction distribution than the other models do. A typical example of

331   this tendency can be observed in the region bounded by the white dotted line in Fig. 9 (a-1), (b-1) and (c-1). In the

332   experimental and simulation results of Model 3, the NO mole fraction in this region is high; whereas for Models 1

333   and 2, it is low. This significant differences between the NO mole fractions of the different models can be explained

334   by the differences in the volatile fuel NO production/reduction characteristics shown in Fig. 2. In this region, the O_2

335   mole fraction is low (Fig. 9 (e-1)) and the gas temperature is high (Fig. 9 (f-1)). As can be seen in Figs. 2 (a) and 2

336   (b), the net NO production rate by the volatile fuel NO mechanism strongly depends on the O_2 mole fraction, i.e.,

337   the net NO production rate by the volatile fuel NO mechanism decreases with increasing O_2 mole fraction; this

338   overall tendency is the same for all three models. However, among the models, there are significant difference in the

339   overall gas temperature trends, as shown in Figs. 2 (e) and 2 (f). The net NO production for Model 3 can be positive

340   if the temperature is high, even if the O_2 mole fraction is low, as shown in Fig. 2 (f). In contrast, that for Models 1

341   and 2 cannot be positive. In other words, for Model 1 and 2, whether the net NO production rate is positive or

342   negative is determined almost exclusively by the O_2 mole fraction; whereas for Model 3, it is determined not only by

343   O_2, but also by gas temperature. This difference between the dependences of the net NO production by the volatile

344   fuel NO mechanism on gas temperature is the main cause for the significant differences between the predicted NO

345   mole fraction distributions. In the region bounded by the white dotted line in Fig. 9, the O_2 mole fraction is low (Fig.

346   9 (e-1)) and the gas temperature is high (Fig. 9 (f-1)); therefore, significant differences between the models in terms

347   of NO mole fraction were observed in this region. Similarly, significant differences among the models in terms of

348   NO mole fractions in the region bounded by the white dotted line are evident in Fig. 9 (a-2), (b-2) and (c-2). In the

349   experimental and simulation results of Model 3, the NO mole fraction in this region is high; whereas for Models 1

350   and 2, it is low. The NO mole fraction around the central axis at $Z > 0.75$ m is low for all of the simulation results,

351   whereas for the experimental results, it is high. However, the simulation results of Model 3 are closer to the

352   experimental results than that of the other models.

353   Figure 10 shows the rates of NO production or reduction by each mechanism on the central axis of the furnace for

354   Case 1. The contributions of the Zeldovich and prompt NO mechanisms to NO production or reduction of NO are

355   quite small. On the other hand, the contribution of volatile fuel NO production is very large compared with that of

356   the other mechanisms. This is why the differences in modeled volatile fuel NO strongly affect the distribution of the

357   NO mole fraction in the furnace. The NO production rate by volatile fuel NO mechanism in Model 3 is greater than

358   that for the other two models. Although the NO reduction rate by volatile fuel NO mechanism in Model 3 is also

359   greater than that for the other two models, the NO mole fraction steeply increases from $Z = 0.6$ to $Z = 0.75$ because

360   of the high volatile fuel NO production rate. The rate of NO reduction by char particles in the results of Model 3 is

361   higher than that for the other two models. This is because the NO concentration in the results of Model 3 is higher

362   than that for the other two models.

363   As discussed above, the model proposed by Mitchell et al. can reproduce the tendency of the measurement results

364   better than the other two models. However, there are some quantitative discrepancies between the simulation results

365   of the model by Mitchell et al. and the experimental results, as observed in Figs. 8 and 9. The main reason of the

366   discrepancies is considered to be the overestimation of NO production rate in high oxygen concentration region. For

367   instance, the calculated NO mole fraction near the furnace wall in Fig 9, in which the O_2 concentration is higher than

368   that near the central axis, is higher than the measured NO mole fraction. The higher NO production rate in the

369   condition of high oxygen concentration for Model 3 compared to other two models can be also confirmed in Fig. 2

370   (a) and (b). Further improvement of the models is required to predict the NO production/reduction characteristics

371   more precisely.

372

373

3.2. Cause of differences between NO conversion ratios of two coals

In Fig. 7, NO emission increases with increasing Wara coal mixing ratio. As previously mentioned, a large portion of the NO emitted from a furnace exit originates from fuel NO mechanisms. Therefore, NO emission depends strongly on the amount of fuel nitrogen fed into the furnace. For this reason, the conversion ratio of fuel nitrogen to NO is widely used as an indicator of the combustion performance of coal against the NO emission. The conversion ratio is defined as follows:

$$CR_{NO} = \frac{EX_{NO}}{F_N} \times 100 , \qquad (3.1)$$

where CR_{NO}, EX_{NO} and F_N are the conversion ratio of fuel nitrogen to NO [%], the NO emission rate at the furnace exit [mol/s], and the fuel nitrogen feeding rate from the burner [mol/s], respectively.

Figure 11 shows CR_{NO} as a function of the Wara coal mixing ratio, revealing that CR_{NO} increases with increasing Wara coal mixing ratio. This indicates that the NO formation/reduction characteristics are affected by the Wara coal mixing ratio. In this section, the cause of the increase in CR_{NO} is discussed using the simulation results of Model 3.

Figure 12 shows a comparison of the two-dimensional distributions of net NO production/reduction rate, NO mole fraction, gas temperature, and O_2 mole fraction for Cases 1 and 4 on the cross section at the center of the furnace. The main gas flow patterns are indicated by the black arrows in the figures. The position of the flame front, which is located at the position where the gas temperature steeply increases, is also indicated by solid white lines. It is found that the position of the flame front for Case 4 is markedly different from that for Case 1. Due to the large flame lift-off, the distance between the flame front and burner exit for Case 4 is larger than that for Case 1. For both cases, a region with a high net NO production rate is accompanied by the flame front (Fig. 12 (a-1) and (a-2)). In Fig. 12 (a-1), for Case 1, there is a region with a high net NO reduction rate immediately downstream of a region with a high net NO production rate. For Case 4, however, there is no region with high net NO reduction rate in downstream of a region with a high net NO production rate, as indicated in Fig. 12 (a-2). Necessary conditions for a high NO reduction rate are a high NO mole fraction, high gas temperature, and low oxygen mole fraction, as can be understood from Eqs. (2.22) and (2.23). The NO reduction rate increases with increases in X_{NO} and T_g in Eq. (2.23). However, when the oxygen mole fraction is high, the net NO production rate is also high because the NO production

15

401   rate, expressed by Eq. (2.22), becomes larger than the NO reduction rate, expressed by Eq. (2.23). For Case 1, all of

402   the necessary conditions for a high NO reduction rate are met in the region with high net NO reduction, i.e., the

403   conditions of a high NO mole fraction (Fig. 12 (b-1)), high gas temperature (Fig. 12 (c-1)), and low oxygen mole

404   fraction (Fig. 12 (d-1)) are satisfied in the region bounded by the white dotted line. For Case 4, on the other hand,

405   although the conditions of a high NO mole fraction (Fig. 12 (b-2)) and high gas temperature (Fig. 12 (c-2)) are

406   satisfied, the condition of low oxygen mole fraction is not satisfied in the region bounded by white dotted lines (Fig.

407   12 (d-2)), which is immediately downstream of the region with a high NO production rate. Whether or not the

408   region with a high NO reduction rate exists is the main cause of the difference between CR_{NO} in Cases 1 and 4, as

409   shown in Fig. 11.

410   From the above discussion, it was found that the formation of a region with a low oxygen mole fraction

411   immediately downstream of a region with a high net NO production rate is the essential condition for low CR_{NO}.

412   This finding should be considered in the development of low NOx burners and the optimization of operating

413   conditions to reduce NOx emission.

414

415   **4. Conclusions**

416   In this study, numerical simulations of the coal combustion field in a 760 kW test furnace were performed by

417   employing three models for fuel NO formation to investigate the effect of fuel NO formation models on the

418   prediction of NO formation/reduction characteristics. The results show significant differences between the NO

419   concentration predictions of the three models. The model proposed by Mitchell et al. could reproduce the tendency

420   of the measurement results better than the models proposed by De Soete and Chen et al. It was found that significant

421   differences between the NO concentration predictions of the models resulted from differences between dependencies

422   of the net NO production rate by the volatile fuel NO mechanism on the gas temperature in the different models.

423   Furthermore, the cause of the difference between the NO conversion ratios of bituminous coal and sub-bituminous

424   coal that contains a high level of moisture was investigated using simulation results obtained using the model of

425   Mitchell et al. It was concluded that the formation of a region with a low oxygen mole fraction immediately

426   downstream of a region with a high net NO production rate is the essential condition for realizing a low NO

427   conversion ratio.

428

References

[1] M. Ikeda, H. Makino, H. Morinaga, K. Higashiyama, JSME Int J Series B 47 (2004) 180-185.

[2] Chen Z, Wang Z, Li Z, Xie Y, Ti S, Zhu Q. Experimental investigation into pulverized-coal combustion performance and NO formation using sub-stoichiometric ratios. Energy 2014;73:844-55.

[3] Wang J, Fan W, Li Y, Xiao M, Wang K, Ren P. The effect of air staged combustion on NOx emissions in dried lignite combustion. Energy 2012;37:725-36.

[4] Liu J, Gao S, Jiang X, Shen J, Zhang H. NO emission characteristics of superfine pulverized coal combustion in the O2/CO2 atmosphere. Energy Conversion Manage 2014;77:349-55.

[5] Warzecha P, Boguslawski A. LES and RANS modeling of pulverized coal combustion in swirl burner for air and oxy-combustion technologies. Energy 2014;66:732-743.

[6] Yeh C, Du S, Tsai C, Yang R. Numerical analysis of flow and combustion behavior in tuyere and raceway of blast furnace fueled with pulverized coal and recycled top gas. Energy 2012;42:233-240.

[7] Modlinski N, Madejski P, Janda T, Szczepanek K, Kordylewski W. A validation of computational fluid dynamics temperature distribution prediction in a pulverized coal boiler with acoustic temperature measurement. Energy 2015;92:77-86.

[8] Belošević S, Tomanović I, Beljanski V, Tucaković D, Živanović T. Numerical prediction of processes for clean and efficient combustion of pulverized coal in power plants. Applied Thermal Eng 2015;74:102-10.

[9] Hwang M, Kim S, Kim G, Lee B, Song J, Park M, Jeon C. Simulation studies on direct ash recycling and reburning technology in a tangentially fired 500 MW pulverized coal boiler. Fuel 2013;114:78-87.

[10] Hashimoto N, Watanabe H. Numerical analysis on effect of furnace scale on heat transfer mechanism of coal particles in pulverized coal combustion field. Fuel Processing Tech 2016;145:20-30.

[11] Hashimoto N, Kurose R, Tsuji H, Shirai H. A numerical analysis of pulverized coal combustion in a multiburner furnace. Energy & Fuels 2007;21:1950-8.

[12] Kurose R, Makino H, Suzuki A. Numerical analysis of pulverized coal combustion characteristics using advanced low-NOx burner. Fuel 2004; 83:693-703.

[13] Kurose R, Ikeda M, Makino H. Combustion characteristics of high ash coal in a pulverized coal combustion. Fuel 2001;80:1447-55.

[14] Kurose R, Tsuji H, Makino H. Effects of moisture in coal on pulverized coal combustion characteristics. Fuel 2001;80:1457-65.

[15] Kurose R, Watanabe H, Makino H. Numerical simulations of pulverized coal combustion. KONA Powder Particle J 2001;27:144-56.

[16] Muto M, Watanabe H, Kurose R, Komori S, Balusamy S, Hochgreb S. Large-eddy simulation of pulverized coal jet flame - Effect of oxygen concentration on NOx formation. Fuel 2015;142:152-63.

[17] Stadler H, Toporov D, Förster M, Kneer R. On the influence of the char gasification reactions on NO formation in flameless coal combustion. Combust Flame 2009;156:1755-63.

[18] Schaffel N, Mancini M, Szlęk A, Weber R. Mathematical modeling of MILD combustion of pulverized coal. Combust Flame 2009;156:1771-84.

[19] Lee B, Song J, Kim R, Kim S, Kim Y, Chang Y, Jeon C. Simulation of the influence of the coal volatile matter content on fuel NO emissions in a drop-tube furnace. Energy & Fuels 2010;24:4333-40.

[20] Taniguchi M, Kamikawa Y, Okazaki T, Yamamoto K, Orita H. A role of hydrocarbon reaction for NOx formation and reduction in fuel-rich pulverized coal combustion. Combust Flame 2010;157:1456-66.

[21] Le Bris T, Cadavid F, Caillat S, Pietrzyk S, Blondin J, Baudoin B. Coal combustion modelling large power plant, for NOx abatement. Fuel 2007;86:2213-20.

[22] Díez LI, Cortés C, Pallarés J. Numerical investigation of NOx emissions from a tangentially-fired utility boiler under conventional and overfire air operation. Fuel 2008;87:1259-69.

[23] Choi CR, Kim CN. Numerical investigation on the flow, combustion and NOx emission characteristics in a 500 MWe tangentially fired pulverized-coal boiler. Fuel 2009;88:1720-31.

[24] Lv Y, Wang Z, Zhou J, Cen K. Full-scale numerical investigation of a selective noncatalytic reduction (SNCR) system in a 100 MW utility boiler with complex chemistry and decoupling approach. Energy & Fuels 2010;24:5432-40.

[25] Zeng L, Li Z, Zhao G, Shen S, Zhang F. Numerical simulation of combustion characteristics and NOx

emissions in a 300 MWe utility boiler with different outer secondary-air vane angles. Energy & Fuels 2010;24:5349-58.

[26] Zhou H, Mo G, Si D, Cen K. Numerical simulation of the NOx emissions in a 1000 MW tangentially fired pulverized-coal boiler: Influence of the multi-group arrangement of the separated over fire air. Energy & Fuels 2011;25:2004-12.

[27] Fang Q, Musa AAB, Wei Y, Luo Z, Zhou H. Numerical simulation of multifuel combustion in a 200 MW tangentially fired utility boiler. Energy & Fuels 2012;26:313-23.

[28] Belosevic S, Beljanski V, Tomanovic I, Crnomarkovic N, Tucakovic D, Zivanovic T. Numerical analysis of NOx control by combustion modifications in pulverized coal utility Boiler. Energy & Fuels 2012;26:425-42.

[29] Pershing DW, Martin GB, Berkau EE. Influence of design variables on the production of thermal and fuel NO from residual oil and coal combustion. AIChE Symp Series 1975;71:19-29.

[30] De Soete GG. Overall reaction rates of NO and N2 formation from fuel nitrogen. Proc Combust Inst 1975;15:1093-102.

[31] Chen W, Smoot LD, Fletcher TH, Boardman RD. A computational method for determining global fuel-NO rate expressions. Part 1. Energy & Fuels 1996;10:1036-45.

[32] Mitchell JW, Tarbell JM. A kinetic model of nitric oxide formation during pulverized coal combustion. AIChE journal 1982;28:302-11.

[33] Baulch DL, Drysdall DD, Horne DG, Lloyd AC. Evaluated Kinetic Data for High Temperature Reactions, Butterworth, 1973.

[34] Westenberg AA. Kinetics of NO and CO in lean, premixed hydrocarbon-air flames. Combust Sci Tech 1971;4:59-64.

combustion. AIChE J 1982;28:302-11.

[35] Pedersen LS, Glarborg P, Dam-Johansen K. A reduced reaction scheme for volatile nitrogen conversion in coal combustion. Combust Sci Tech 1998;131:193-223.

[36] Haynes BS. Reactions of ammonia and nitric oxide in the burnt gases of fuel-rich hydrocarbon-air flames. Combust Flame 1977;28:81-91.

[37] Lockwood FC, Romo-Millares CA. Mathematical modeling of fuel-NO emissions from PF burners. J Inst Energy 1992;65:144-52.

[38] Aarna I, Suuberg EM. A review of the kinetics of the nitric oxide-carbon reaction. Fuel 1997;76:475-91.

[39] Hahn WA, Shadman F. Effect of solid Structural change on the rate of NO formation during char combustion. Combust Sci Tech 1983;30:89-104.

[40] Levy JM, Chan LK, Sarofim AF, Beer JM. NO/char reactions at pulverized coal flame conditions. Proc Combust Inst 1981;18:111-20.

[41] Schönenbeck C, Gadiou R, Schwartz D. A kinetic study of the high temperature NO–char reaction. Fuel 2004;83:443-50.

[42] Turns SR. An introduction to combustion: Concepts and applications. 3rd ed. New York: McGraw-Hill; 2012, p. 120-1.

[43] Hashimoto N, Shirai H. Numerical simulation of sub-bituminous coal and bituminous coal mixed combustion employing TDP model. Energy 2014;71:399-413.

[44] Yakhot V, Orszag SA. Renormalization group analysis of turbulence. I. Basic theory. J Scientific Computing 1986;1:3-51.

[45] Siegel R, Howell J. Thermal Radiation Heat Transfer. 4th ed. New York: Taylor & Francis; 2002, p. 681-95.

[46] Magnussen BF, Hjertager BH. On mathematical modeling of turbulent combustion with special emphasis on soot formation and combustion. Proc Combust Inst 1977;16:719-29.

[47] Field MA. Rate of combustion of size-graded fractions of char from a low-rank coal between 1200°K and 2000°K. Combust Flame 1969;13:237-52.

[48] Essenhigh RH, Klimesh HE, Förtsch D. Combustion characteristics of carbon: Dependence of the Zone I-Zone II transition temperature (T_c) on particle radius. Energy & Fuels 1999;13:826-31.

[49] Gosman AD, Ioannides E. Aspects of computer simulation of liquid-fuelled combustors. AIAA paper 1981: No. 81-0323.

[50] Issa RI, Solution of the implicitly discretised fluid flow equations by operator-splitting. Comp Phys 1986;62:40-65.

[51] Crowe CT, Sharma MP, Stock DE. Particle-source-in cell (PSI-cell) model for gas-droplet flows. Trans ASME J Fluids Eng 1977;99:325-32.

[52] Niksa S. Predicting the devolatilization behavior of any coal from its ultimate analysis. Combust Flame 1995;100:384-94.

[53] Niksa S, Kerstein AR. FLASHCHAIN theory for rapid coal devolatilization kinetics. 1. Formulation. Energy & Fuels 1991;5:647-65.

[54] Westbrook CK, Dryer FL. Simplified reaction mechanisms for the oxidation of hydrocarbon fuel in flames. Combust Sci Tech 1981;27:31-43.

[55] Hautman DJ, Dryer FL, Schug KP, Glassman I. A multiple-step overall kinetic mechanism for the oxidation of hydrocarbons. Combust Sci Tech 1981;25:219-35.

[56] Ikeda M, Makino H, Morinaga H, Higashiyama K, Kozai Y. Emission characteristics of NOx and unburned carbon in fly ash during combustion of blends of bituminous/sub-bituminous coals. Fuel 2003;82:1851-7.

Figure and table captions

Fig. 1. Schematics of reaction models for NO originating from volatile matter.

Fig. 2. Comparison of NO production/reduction rates between three volatile fuel NO models

Fig. 3. Computational domain.

Fig. 4. Diameter distribution of coal particles used in the experiment [56].

Fig. 5. Gas velocity vectors and distributions of gas temperature and O_2 mole fraction for Case 1 (100% Newlands) and Case 4 (100% Wara).

Fig. 6. Effect of C_1 in Eq. (2.25) for Model 3 on NO mole fraction at furnace exit.

Fig. 7. NO mole fraction at furnace exit versus Wara coal mixing ratio.

Fig. 8. Distributions of NO mole fraction on central axis of furnace.

Fig. 9. Distributions of NO mole fraction for Case 1 (100% Newlands) and Case 4 (100% Wara).

Fig. 10. NO production/reduction rate on central axis of furnace (Case 1).

Fig. 11. NOx conversion ratio as versus Wara coal mixing ratio.

Fig. 12. Comparison of distributions of NO production/reduction rate, NO mole fraction, gas temperature and O_2 mole fraction for Case 1 (100% Newlands) and Case 4 (100% Wara).

Table 1 NO formation/reduction model.

Table 2 Summary of mathematical models used in simulations.

Table 3. Coal properties.

Table 4. Cases investigated in this study.
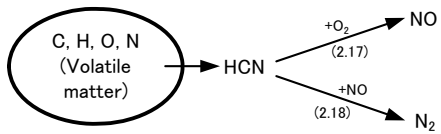
(a) Model proposed by De Soete.
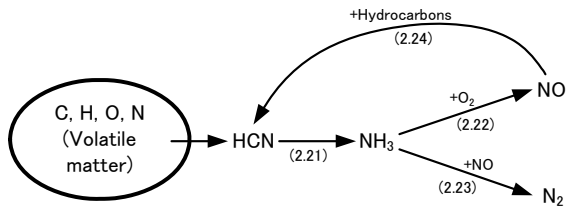
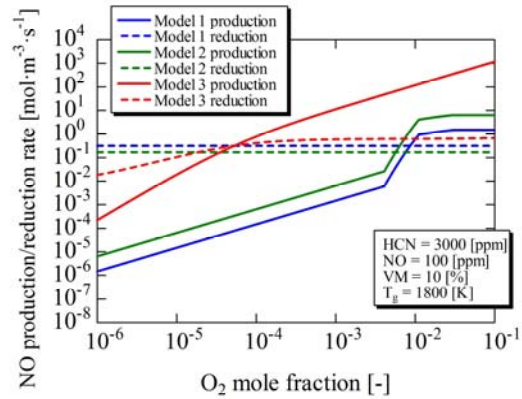(b) Model proposed by Mitchell et al.

Fig. 1. Schematics of reaction models for NO
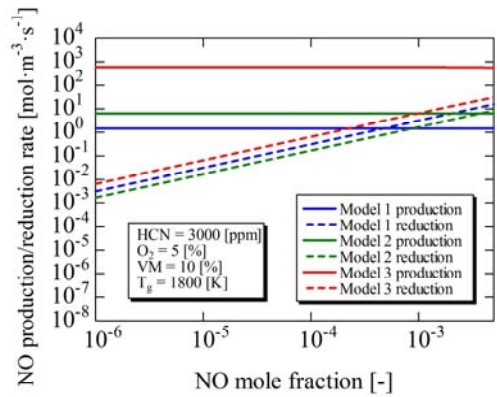
originating from volatile matter.
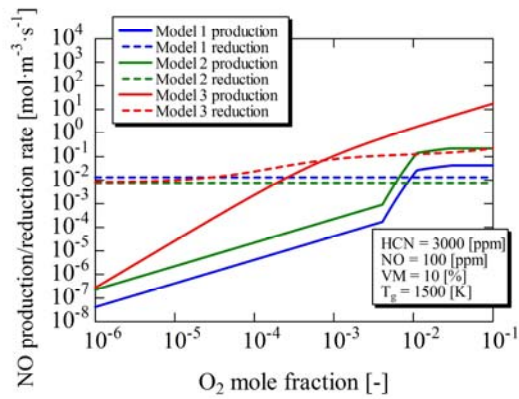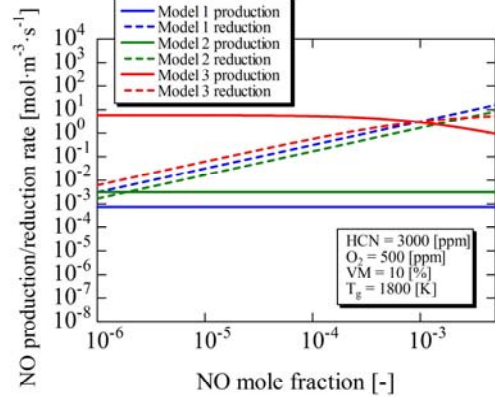
(a) NO production/reduction rate as a function of O₂ mole fraction at temperature of 1500 K

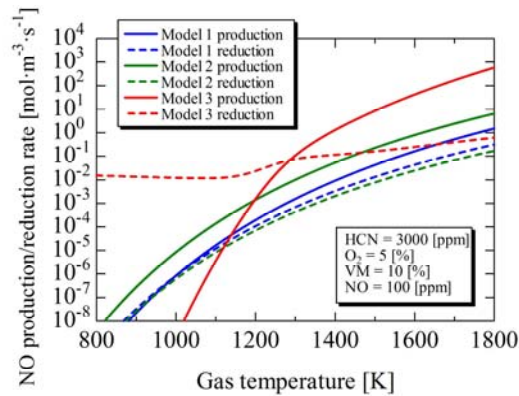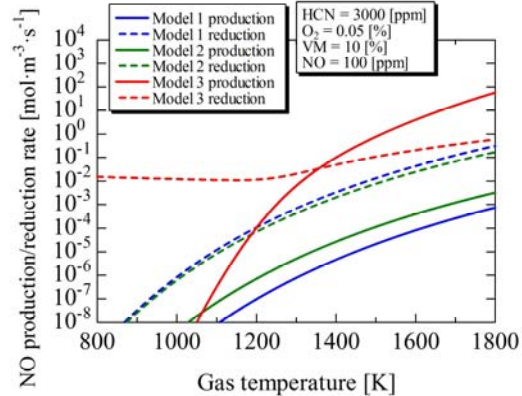(b) NO production/reduction rate as a function of O₂ mole fraction at temperature of 1800 K

(c) NO production/reduction rate as a function of NO mole fraction at O₂ concentration of 5%

(d) NO production/reduction rate as a function of NO mole fraction at O₂ concentration of 500 ppm

(e) NO production/reduction rate as a function of gas temperature at O₂ concentration of 5%

(f) NO production/reduction rate as a function of gas temperature at O₂ concentration of 500ppm

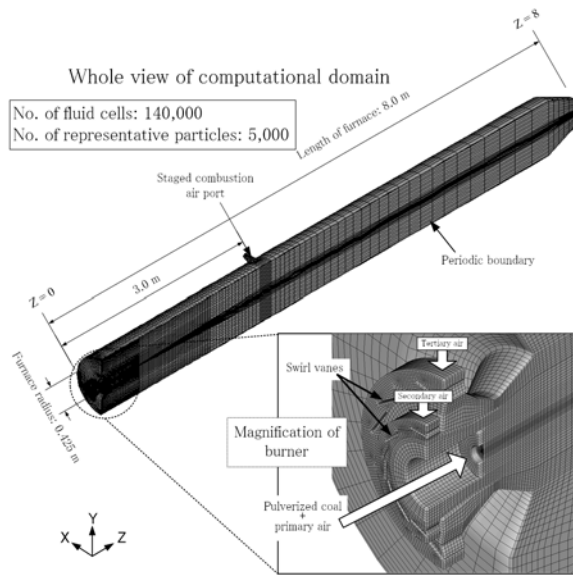Fig. 2. Comparison of NO production/reduction rates between three volatile fuel NO models.
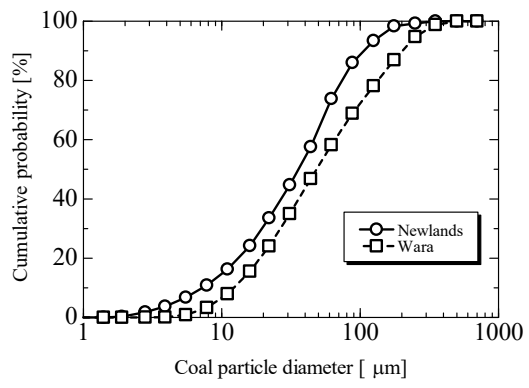
Whole view of computational domain

No. of fluid cells: 140,000
No. of representative particles: 5,000

Z = 8

Length of furnace: 8.0 m

Staged combustion
air port

Periodic boundary

Z = 0

3.0 m

Furnace radius: 0.425 m

Tertiary air

Swirl vanes

Secondary air

Magnification of
burner

Pulverized coal
+
primary air

X Y Z

Fig. 3. Computational domain.

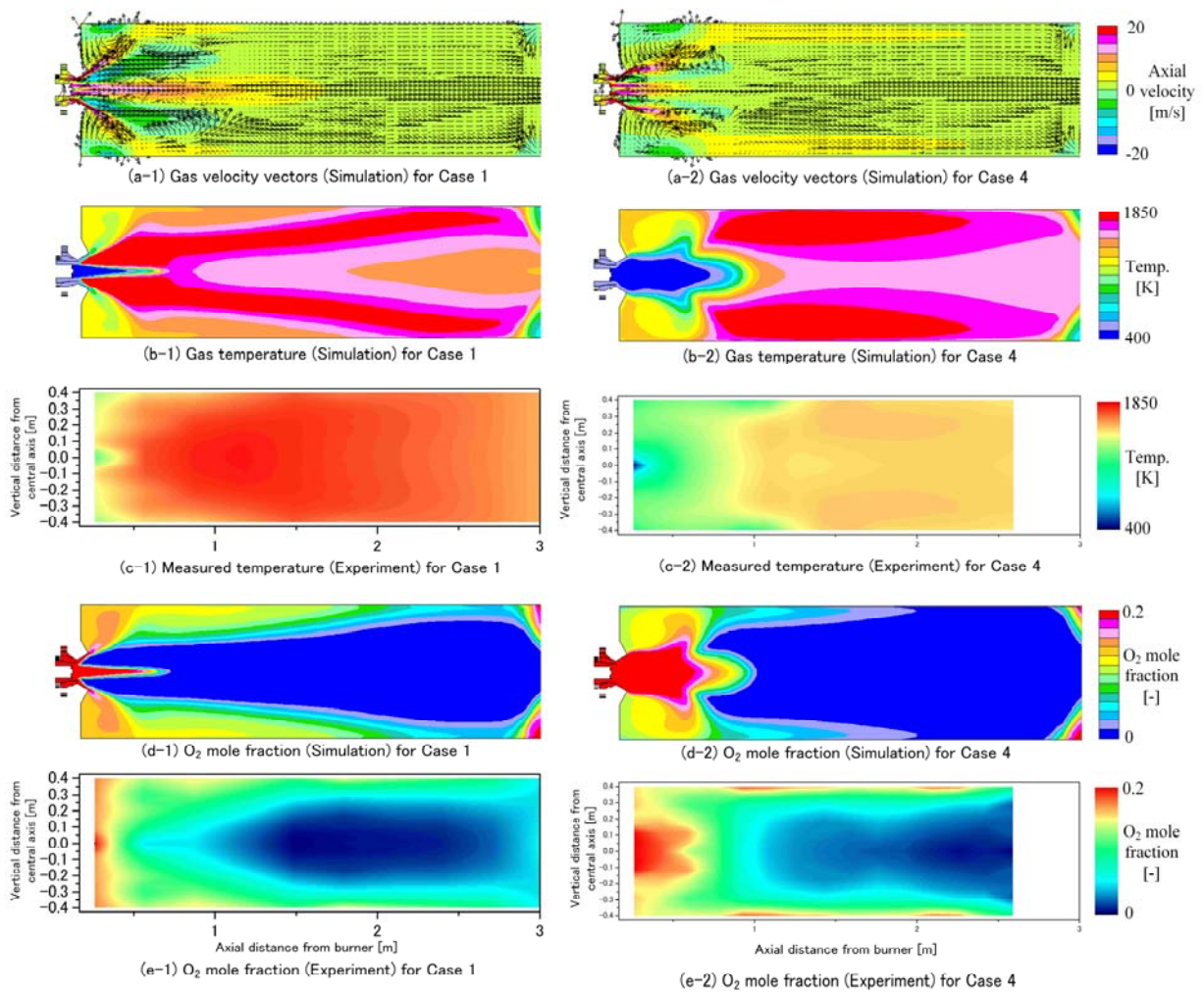Fig. 4. Coal particle diameter distribution of used

in the experiment [56].

Fig. 5. Gas velocity vectors and distributions of gas temperature and O_2 mole fraction for Case 1 (100% Newlands) and Case 4 (100% Wara).
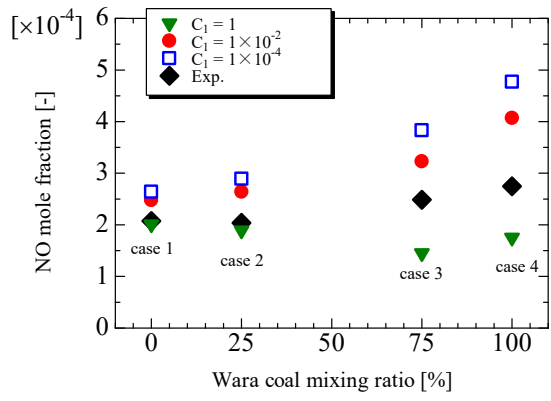
Fig. 6. Effect of C_1 in Eq. (2.25) for Model 3 on
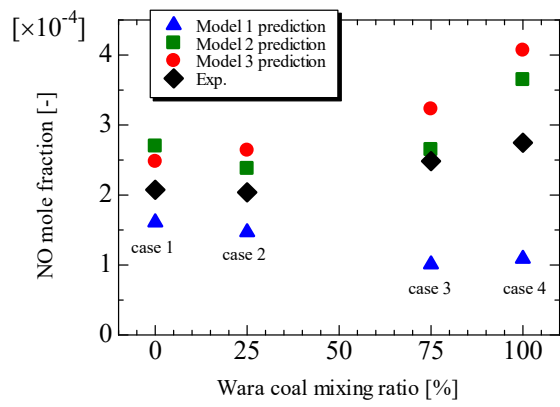
NO mole fraction at furnace exit.

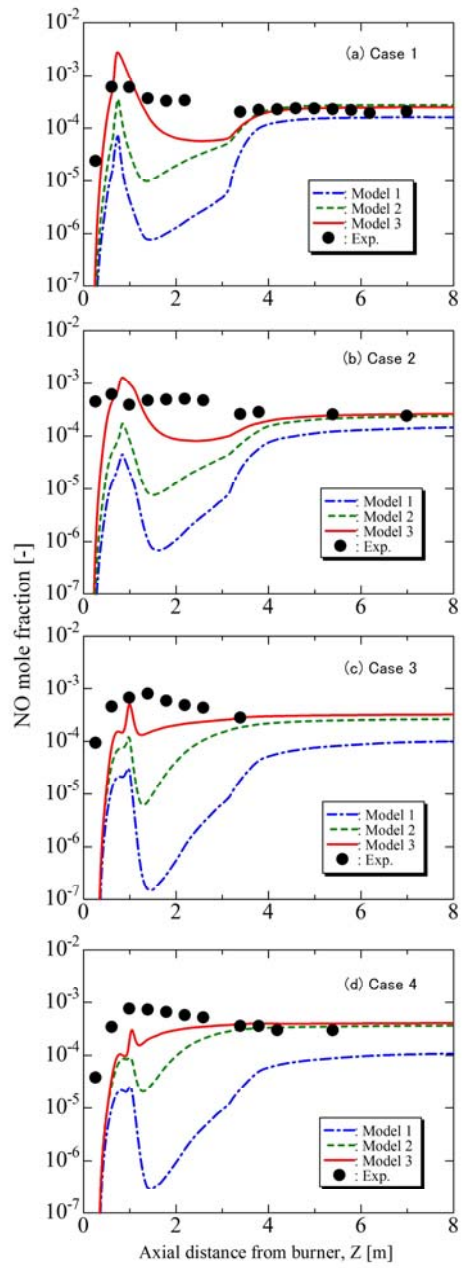Fig. 7. NO mole fraction at furnace exit versus

Wara coal mixing ratio.

Fig. 8. Distributions of NO mole fraction on
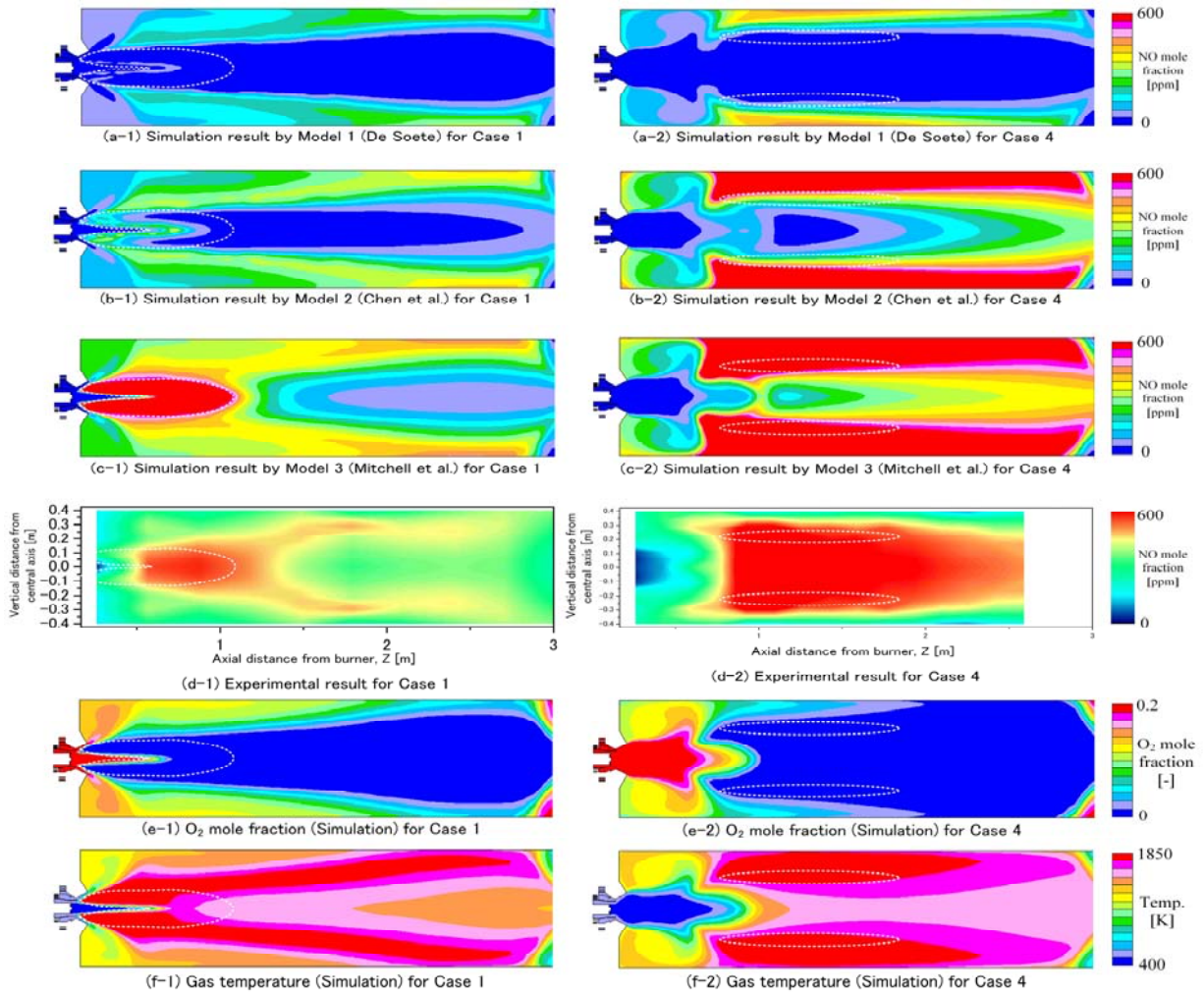central axis of furnace.

Fig. 9. Distributions of NO mole fraction for Case 1 (100% Newlands) and Case 4 (100% Wara).
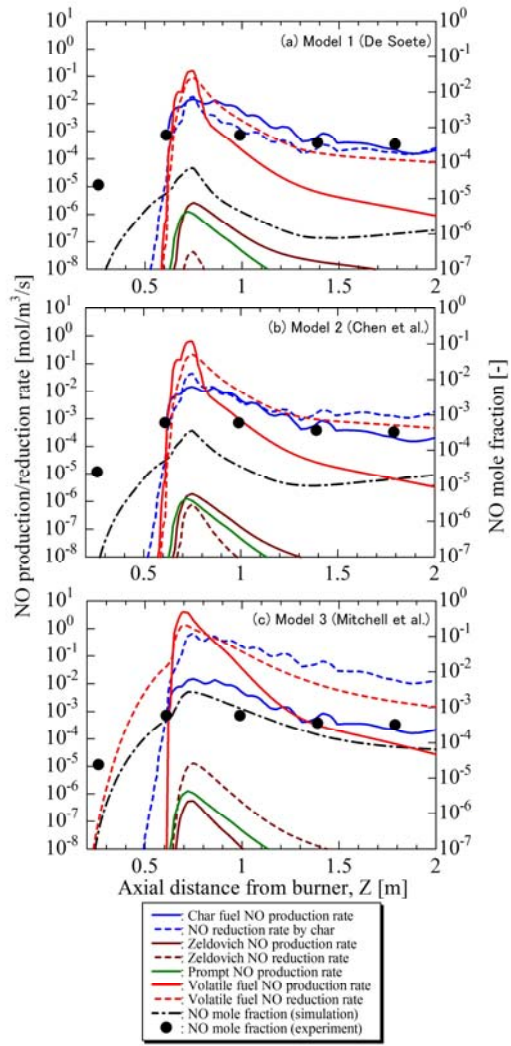
Fig. 10. NO production/reduction rate on central axis of furnace (Case 1).
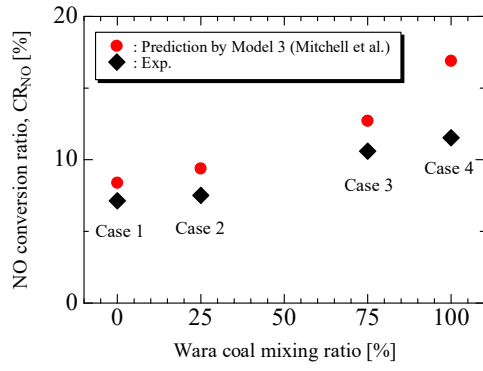
Fig. 11. NOx conversion ratio as versus Wara

coal mixing ratio.

(a-1) Net NO production rate with gas velocity vectors for Case 1

(a-2) Net NO production rate with gas velocity vectors for Case 4

(b-1) NO mole fraction with gas velocity vectors for Case 1

(b-2) NO mole fraction with gas velocity vectors for Case 4

(c-1) Gas temperature with gas velocity vectors for Case 1

(c-2) Gas temperature with gas velocity vectors for Case 4

(d-1) O_2 mole fraction with gas velocity vectors for Case 1

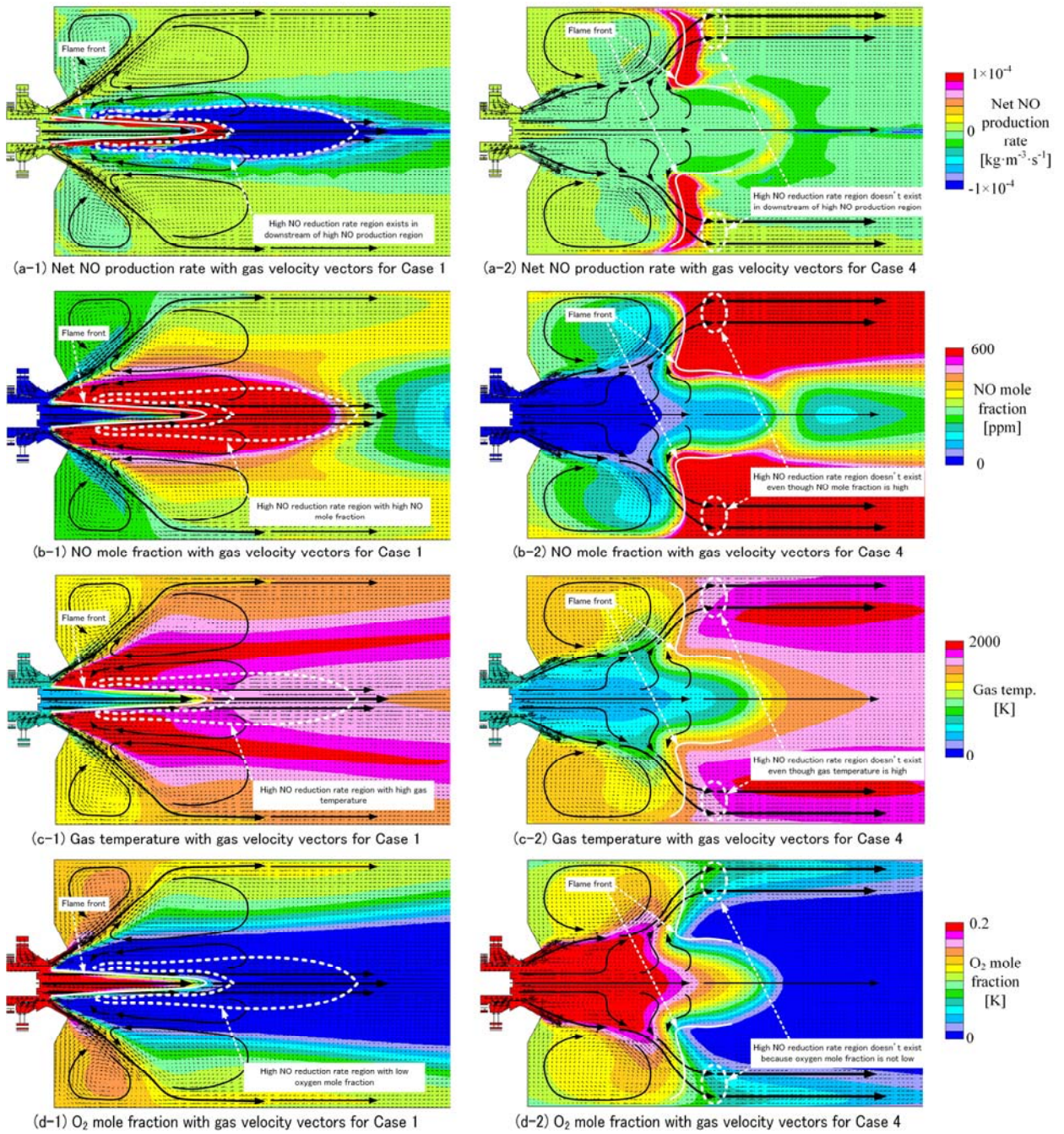(d-2) O_2 mole fraction with gas velocity vectors for Case 4

Fig. 12. Comparison of distributions of NO production/reduction rate, NO mole fraction, gas temperature and O_2 mole fraction for Case 1 (100% Newlands) and Case 4 (100% Wara).

Table 1. NO formation/reduction model.

Model No.	Zeldovich NO	Prompt NO	Volatile fuel NO	Char fuel NO
Model 1			Eqs. (2.17)&(2.18) (De Soete)	
Model 2	Eqs. (2.1)-(2.11)	Eqs. (2.12)-(2.16)	Eqs. (2.19)&(2.20) (Chen et al.)	Eqs. (2.26)&(2.27)
Model 3			Eqs. (2.21)-(2.25) (Mitchell et al.)	

Table 2. Summary of mathematical models used in simulations.

Phenomena	Mathematical model
Turbulence	RNG k-ε [44]
Thermal Radiation	Discrete Ordinate [45]
Devolatilization	Modified TDP model [43]
Gas phase combustion	Combined model of kinetics and eddy dissipation [46]
Char combustion	Field et al. [47]
Char combustion zone transition	Essenhigh et al. [48]
Particle's tracking	Lagrangian
Turbulence effect on particle motion	Stochastic [49]

Table 3. Coal properties.

Coal	Newlands	Wara
Proximate analysis [wt%]		
Moisture* (as-received)	2.5	41.2
Moisutre (after pulverized)	0.0	40.1
Volatile matter*	26.6	51.4
Fixed carbon*	58.0	46.5
Ash*	15.4	2.1
Fuel ratio [-]	2.18	0.90
Ultimate analysis* [wt%]		
C	69.6	67.0
H	4.8	5.2
N	1.6	1.2
O	8.2	23.9
Combustible sulfur	0.41	0.63
Lower heating value (LHV)* [MJ/kg]	27.13	25.20
Mass fraction of particles [%]		
D_p = 5 µm	6.8	0.9
D_p = 20 µm	26.8	23.2
D_p = 40 µm	24.0	22.8
D_p = 60 µm	16.3	11.4
D_p = 80 µm	12.2	10.6
D_p = 100 µm	14.0	31.2

*: Dry basis

Table 4. Cases investigated in this study.

Case No.	Coal feeding rate ratio on LHV basis (%)	
	Newlands coal	Wara coal
Case 1	100	0
Case 2	75	25
Case 3	25	75
Case 4	0	100